Supplementary Information to "Dynamical decoding of the competition between charge density waves in a kagome superconductor"

Honglie Ning,[1, *] Kyoung Hun Oh,[1, *] Yifan Su,[1, *] Alexander von Hoegen,[1] Zach Porter,[2, 3, 4] Andrea Capa Salinas,[4] Quynh L Nguyen,[2] Matthieu Chollet,[2] Takahiro Sato,[2] Vincent Esposito,[2] Matthias C Hoffmann,[2] Adam White,[2] Cynthia Melendrez,[2] Diling Zhu,[2] Stephen D Wilson,[4] and Nuh Gedik[1, †]

[1]*Department of Physics, Massachusetts Institute of Technology, Cambridge, MA 02139*
[2]*Linac Coherent Light Source, SLAC National Accelerator Laboratory, Menlo Park, CA, 94025*
[3]*Stanford Institute for Materials and Energy Sciences, Stanford University, Stanford, CA 94305*
[4]*Materials Department, University of California, Santa Barbara, CA 93106*

Contents

Supplementary Note 1. Structure factor calculations

In order to simulate the peak intensity, we calculate the structure factor (S), which is proportional to the square root of the peak intensity. Without considering any charge density wave (CDW)-induced lattice distortion, S can be expressed as:

$$S = \Sigma_j f_j \exp(2\pi i(\mathrm{H}x_j + \mathrm{K}y_j + \mathrm{L}z_j)), \tag{1}$$

where H, K, L are Miller indices for a diffraction peak, x_j, y_j, z_j are the positions of the j-th atom in a unit cell, and f_j is an atomic form factor that depends on (H K L). Here, we only consider in-plane V-V bond distortions within the two kagome planes, because they are the leading lattice instabilities that generate the CDW as predicted by theories and demonstrated by X-ray diffraction measurements [1, 2].

As mentioned in the main text, the two candidates for the $2\times2\times2$ CDW structure are the MLL (and its symmetry-equivalent nematic domains, i.e. LML, LLM) and LLL structures, formed by a combination of one M distortion and two L distortions and three L distortions along three directions $120°$ apart from each other, respectively. The modified S due to the CDW formation can be easily calculated by counting all the V atoms in the expanded unit cell and substituting $x_j \rightarrow x_j + \delta x_j$ and $y_j \rightarrow y_j + \delta y_j$, where δx_j and δy_j correspond to the distortion induced by the V-V bond contraction. In this simulation, we assume that the relative V-V bond distortion is about 0.5% compared to the undistorted bond length for all M and L distortions [3]. The simulation results of the CDW superlattice peak intensity in the (0 K L) plane are shown in Supplementary Figure 1. Although both MLL and LLL phases can plausibly create all half-integer (H K L) peaks since both structures induce a $2 \times 2 \times 2$ unit cell expansion, S calculation shows that in the LLL structure, the peak intensity at (0 -1.5 2.5) (red circle) accidentally vanishes as the S from the upper and lower kagome plane cancels each other. On the other hand, the peak intensity at (0 -1.5 3) (green circle) in the LLL structure is similar to that of the MLL structure, so this peak could originate from both the MLL and LLL structures. Lastly, the peak at (-0.5 -1 2) is also predominantly contributed by the MLL structure, albeit not shown here. The above statement is qualitatively true even if we consider the LLL (85%)$+MMM$ (15%) structure evidenced by recent ARPES experiments [4] rather than the pure LLL structure: the peak intensity at (0 -1.5 2.5) and (-0.5 -1 2) are at least two orders of magnitude smaller in $LLL+MMM$ than in MLL, while the intensity at (0 -1.5 3) is on the same order for both structures. Note that $LLL + MMM$ is actually a single homogeneous phase without domain structures. It represents a structure very similar to LLL, with the only disparity being that the amount of distortion in the inverse star of David and star of David is different. One could also argue that the proportion of the LLL phase may be several orders of magnitude larger than that of the MLL. However, this is inconsistent with any previous static X-ray diffraction measurements, which all provide evidence of MLL. If LLL were dominant, X-ray should manifest features of its presence. We therefore conclude that (0 -1.5 2.5) and (-0.5 -1 2) indeed are predominantly contributed by MLL. Since the three CDW peaks may originate from different CDW structures, it is possible to track the responses of various CDWs by monitoring different peaks.
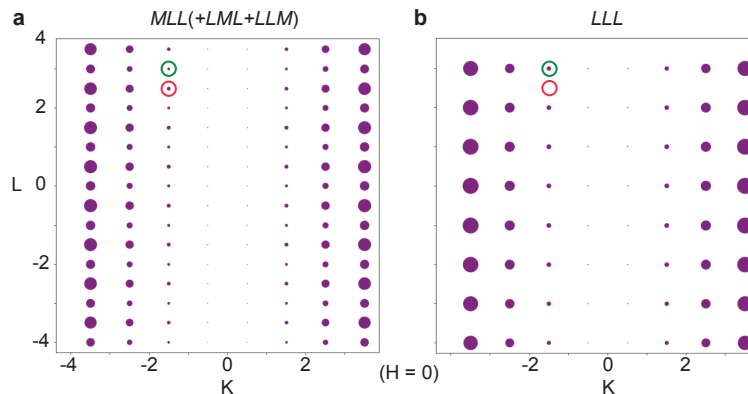
Supplementary Figure 1. **Structure factor calculation results for CDW satellite peaks.** Calculated (0 K L) CDW superlattice peak intensity map of **a**, the MLL (and its symmetry-equivalent nematic domains LML, LLM) and **b**, the LLL structures. The red and green circles denote the peaks at (0 -1.5 2.5) and (0 -1.5 3.0) studied in this work, respectively. We neglect the Bragg peaks for simplicity.
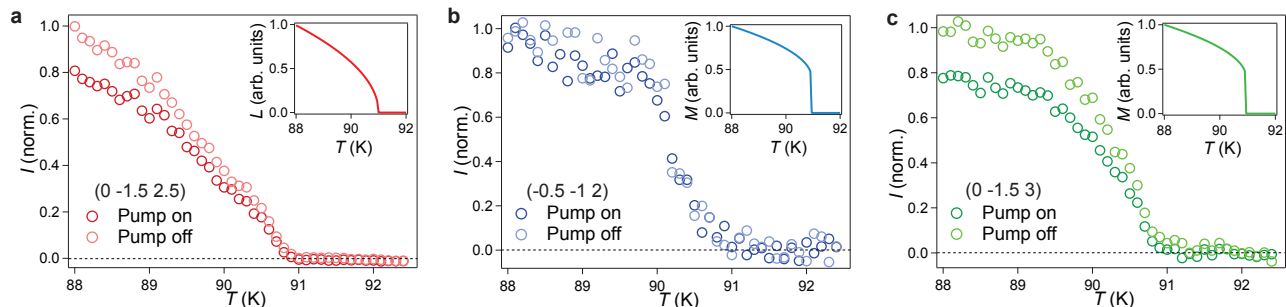
Supplementary Note 2. Temperature dependence of the CDW peak intensity

We first scrutinize the static CDW peak intensity as a function of temperature T close to the CDW transition temperature T_c at the three peak positions (0 -1.5 2.5), (-0.5 -1 2), and (0 -1.5 3). We observe that nonzero intensity at the CDW reciprocal lattice vectors only appears below $T_c = 91$ K. We note that the peak intensity is only one to two orders of magnitude larger than the background given our experimental geometry and accumulation time, demonstrating the relatively weak CDW peak intensity [5]. Above $T_c = 91$ K, we detect no diffuse scattering at these three peak positions within our signal-to-noise ratio.

We note that although previous X-ray diffraction studies have reported the temperature dependence of selected CDW peaks, their temperature step is usually on the order of 1 K or larger [5–10]. In contrast, we conduct a temperature scan with a finer step of 0.1 K and within a narrower range around T_c, allowing us to better resolve the critical behavior of different peaks. We also note that the Bragg conditions which are fulfilled at 88 K almost hold for the entire temperature range. Our careful measurements show that the L = half integer peaks exhibit a smoother intensity onset as temperature decreases compared to the two L = integer peaks (Supplementary Figure 2). As discussed in the main text, the former is mainly contributed by the L order parameter, while the latter peaks are contributed by both L and M order parameters. As later shown in Note 7, L exhibits a second-order phase transition while M depicts a first-order transition at T_c, when they are not coupled (insets of Supplementary Figure 2). These differences provide an explanation for the distinct critical temperature dependence around T_c of different peaks with different indices and lay the foundation of their decoupling upon pumping.

We then unblock the pump and measure the peak intensity at different temperatures at a time delay $t = 0.5$ ps with a pump pulse at $F = 1.5$ mJ/cm^2. The peaks at (0 -1.5 2.5) and (0 -1.5 3) show an obvious intensity drop upon pumping at all temperatures below T_c (Supplementary Figures 2a and 2c), with relative amplitudes similar to those measured at 30 K. The change in intensity of the peak at (-0.5 -1 2) is less apparent (Supplementary Figure 2b), also in agreement with its much smaller change at 30 K compared to the other two peaks.

It is worth noting that T_c does not change within our experimental resolution even when the pump laser is turned on, indicating negligible pump-induced heating at least around T_c. Since the heat capacity is just three times smaller at 30 K compared to that at 90 K [11], the heating at 30 K should be three times larger than that at 90 K and thus also marginal.

Supplementary Figure 2. **Temperature-dependence of the integrated intensity of CDW peaks near T_c.** The integrated intensity as a function of temperature for **a**, the peak at (0 -1.5 2.5), **b**, the peak at (-0.5 -1 2), and **c**, the peak at (0 -1.5 3) both in the presence and absence of a pump at $F = 1.5$ mJ/cm^2 acquired at $t = 0.5$ ps. Landau theory simulations of the temperature dependence of L (second-order) and M (first-order) are depicted in the inset.

Supplementary Note 3. Rocking curve scans with and without pump

We scanned the rocking curve around the Bragg position of each peak by rotating the μ angle of the six-circle diffractometer [12] with a 0.02° step to find the optimal Bragg condition that maximizes the peak intensity. As shown in Supplementary Figure 3, upon light impingement, the peak intensity uniformly decreases without any noticeable peak shift, indicating a predominant melting of the CDW order. This holds true for all the CDW satellite peaks investigated throughout the experiment. The uniform intensity drop across the μ range indicates that the significant difference in the intensity drop for the three CDW peaks is not an artifact caused by light-induced deviations from the exact Bragg condition.
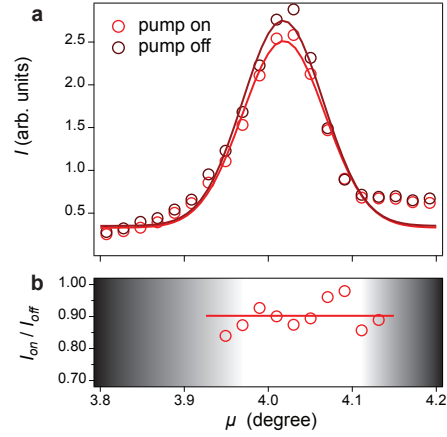
Supplementary Figure 3. **Rocking curves for the CDW peak at (0 -1.5 2.5) in the presence and absence of pumping.** **a**, Rocking curves taken at $t = 0.5$ ps with (light red) and without (dark red) a pump at $F = 1$ mJ/cm^2. The solid lines are fits to Gaussians. **b**, Relative light-induced intensity change, which is nearly a constant as shown by the solid line around the unshaded peak region.

Supplementary Note 4. Momentum dependence of the CDW peak dynamics

Previous tr-XRD studies have reported various possible momentum-(q) dependent dynamics of CDW. For example, in the cuprate superconductor $La_{2-x}Ba_xCuO_4$, the recovery time of the intensity close to the CDW superlattice peak exhibits a q^2-dependence, indicating diffusive CDW dynamics [13]. Meanwhile, in the case of a rare-earth tritelluride, q-dependent dynamics reflecting the formation of CDW domain walls have been observed [14]. To test whether the aforementioned physics occurs in CsV_3Sb_5, we analyze the q-dependence of the CDW peak dynamics. As shown in Supplementary Figure 4, we find that along both $q_{//}$ and $q_\perp$ directions, the CDW melting and recovery dynamics of the peak at (0 -1.5 2.5) do not show noticeable q-dependence upon a pump at $F = 2.5$ mJ/cm^2. The q-independence of the CDW dynamics indicates that neither diffusive behavior nor ultrafast domain wall formation is related to our system. However, we do notice that the magnitude of suppression is more significant at larger q away from the CDW diffraction peak, suggesting that the peak width is reduced upon photo-excitation. It is also worthy noting that this phenomenon is more apparent along $q_\perp$ than $q_{//}$, demonstrating a more significant decrease of width in the out-of-plane direction, in agreement with the conclusion we draw in the main text.
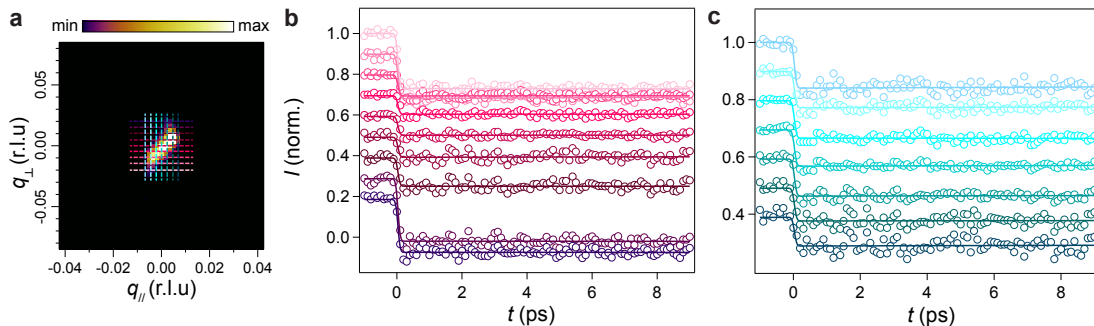
Supplementary Figure 4. **Temporal evolution of different momentum cuts of the CDW peak at (0 -1.5 2.5). a**, Raw image of the (0 -1.5 2.5) superlattice peak before pumping. Colorscale indicates corresponding counts on the detector. The red and blue dashed lines denote the momentum space cuts along the $q_{//}$ and $q_\perp$ directions as shown in panels **b** and **c**, respectively. **b**, Temporal evolution of different $q_\perp$ cuts around the CDW peak at (0 -1.5 2.5) acquired at $F = 2.5$ mJ/cm^2. **c**, Temporal evolution of different $q_{//}$ cuts around the CDW peak at (0 -1.5 2.5) acquired at $F = 2.5$ mJ/cm^2. Solid lines are fits to a single-exponential decay. Curves are displaced vertically for clarity.

Supplementary Note 5. Fluence dependence of the coherent oscillation

We closely examine the oscillation that appears exclusively in the peak at (0 -1.5 2.5) as a function of pump fluence F. The oscillatory components of the peak intensity time traces at various F are depicted in Supplementary Figure 5a, and their fast Fourier transform (FFT) spectra are shown in Supplementary Figure 5b. A single peak at around 1.3 THz can be seen at all F, while at the lowest fluence, another peak may emerge at around 3.1 THz. Both modes have been detected before in transient reflectivity and polarization rotation measurements at lower fluences [15–17].

We focus on the 1.3 THz mode since it shows up in every trace. We fit the traces shown in Supplementary Figure 5a with a single-damped sinusoid $A \exp(-t/\tau) \sin(2\pi f t + \phi)$, where A, τ, f, and ϕ are the amplitude, lifetime, frequency, and phase of the mode, respectively. As shown in Supplementary Figure 5c, f does not exhibit softening despite the CDW melting, consistent with the absence of phonon softening observed previously by inelastic X-ray scattering and Raman spectroscopy [3, 7, 18]. On the other hand, A shows an initial increase with F and then saturates at around $F = 0.5$ mJ/cm^2 (Supplementary Figure 5d). We note that a data point representing zero amplitude at zero pump fluence is included in the plot to depict the trend clearly.

We would like to comment on the nature of this mode. Previous optical measurements demonstrate that this mode exclusively emerge below T_c, suggesting its direct connection to the CDW. Since its frequency matches the frequency of a Cs motion calculated by density functional theory (DFT), the authors assign it to the zone-folded coherent phonon involving Cs motion [15]. However, previous DFT theories and X-ray diffraction measurements also demonstrate a minor effect of Cs motion on the formation of CDW [1, 2]. From this perspective, it is less likely that a coherent Cs motion strongly modulates the CDW superlattice peak which arises predominantly from V displacements. On the other hand, the frequency of this mode is very close to the lowest acoustic phonon energy at the CDW reciprocal lattice vector before zone-folding and shows no softening upon temperature changes [3, 7, 18]. Therefore, it is also possible that this mode is the amplitude mode of MLL, which does not soften, signifying its unconventional nature. We note that this does not contradict the recent angle-resolved photoemission results, where the amplitude modes of the LLL phase are found and indeed exhibit softening with F [19]. Although our results cannot conclusively determine the origin of this mode, further investigation is required to understand its unusual behavior. Nevertheless, regardless of its nature, our main conclusion remains unchanged. Without loss of generality, in the time-dependent Landau theory (TDLT) simulations in Note 7, we treat this mode as a linearly coupled phonon.
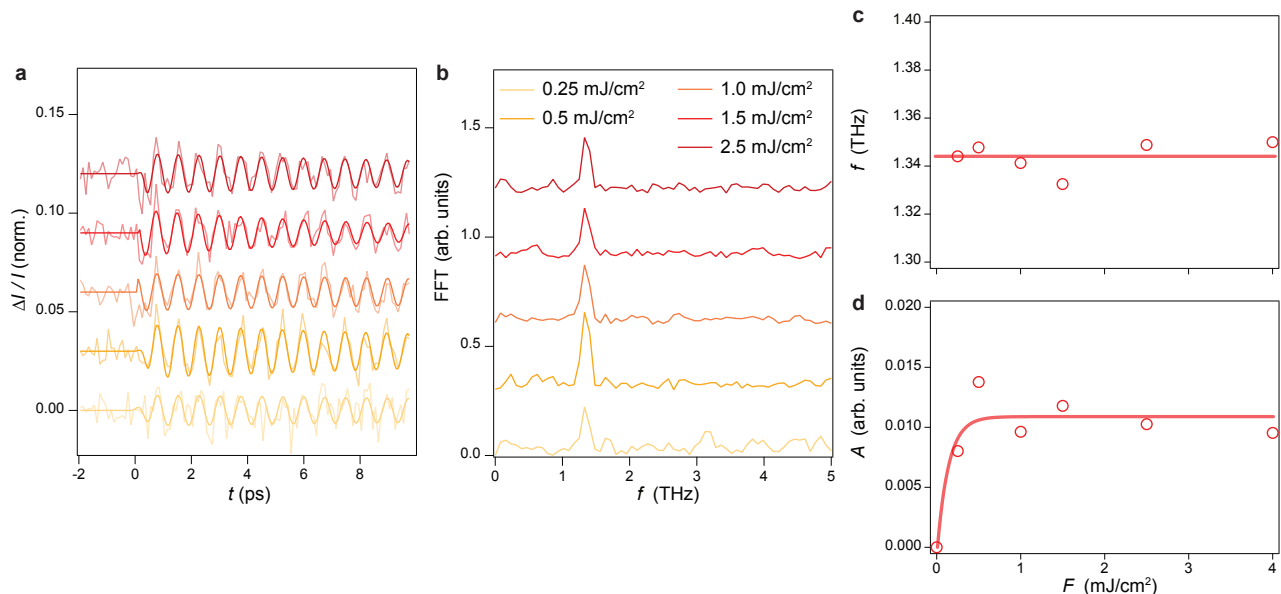
Supplementary Figure 5. **Fluence dependence of the coherent oscillation. a**, Temporal evolution of the integrated intensity of the peak at (0 -1.5 2.5) subtracted by the single exponential decay background at various pump fluences. Fits to damped sinusoids are overlaid atop the data. Curves are offset for clarity. **b**, Fourier transform spectra of the curves in panel **a**. Curves are offset for clarity. **c**, Fluence dependence of the coherent oscillation frequency. **d**, Fluence dependence of the coherent oscillation amplitude. Solid lines are guides to eyes. A data point representing zero amplitude at zero pump fluence is included to depict the trend clearly.

Supplementary Note 6. Temporal evolution of the structural Bragg peaks

The temporal evolution of two Bragg peaks at (0 0 1) and (0 -1 3) upon photo-excitation is shown in Supplementary Figure 6. By integrating the pixels where the Bragg peak is located and subtracting the background, we can obtain the peak intensity change ΔI as a function of time delay t. We can also fit the integrated linecut of the two peaks with a Gaussian along both $q_{//}$ and $q_{\perp}$ directions to obtain their full width at half maximum (FWHM) $\sigma_{//}$ and $\sigma_{\perp}$ as a function of t. In the short timescale $t < 10$ ps, we do not observe any prominent change in peak intensity and peak width within our signal-to-noise ratio (Supplementary Figure 6), in contrast to the melting and sharpening (broadening) of CDW peaks. We indeed observe that the intensity of the peak at (0 0 1) exhibits a slow decrease in the long timescale spanning several hundreds of picoseconds under $F = 6$ mJ/cm^2, which can be understood as the Debye-Waller effect arising from heating. However, this effect only appears at a relatively long timescale and at fluences higher than the range where we focus on. Therefore, we can conclude that all the transient changes in peak intensity and width of the CDW peaks are nonthermal.
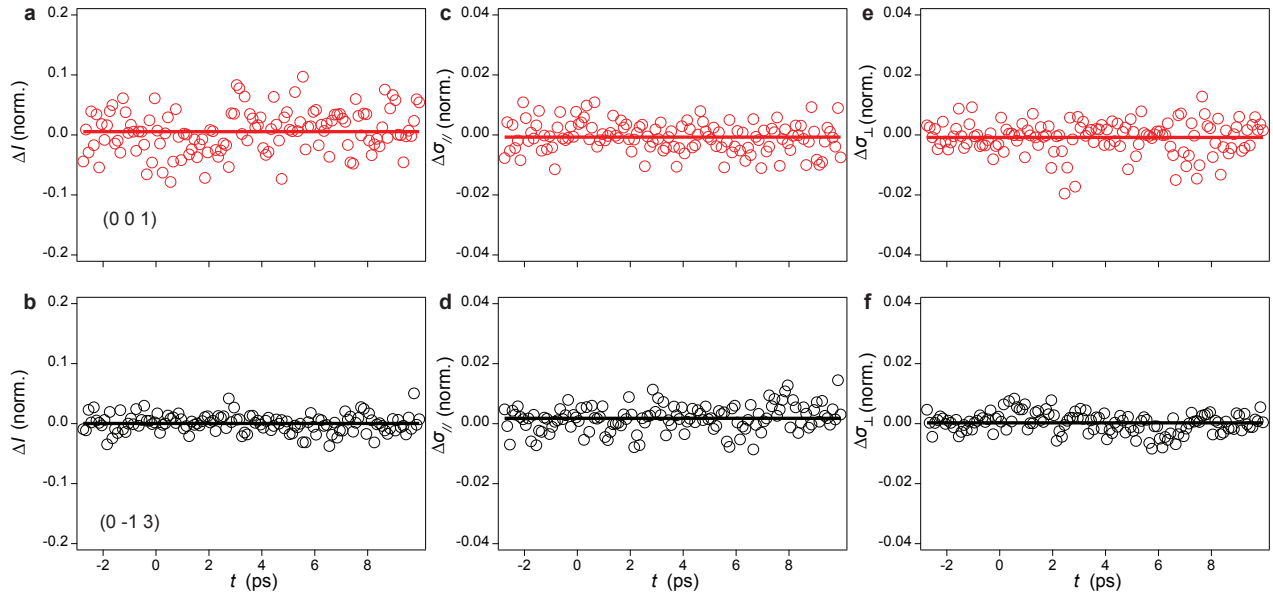
Supplementary Figure 6. **Temporal evolution of the intensity and width of structural Bragg peaks. a,b**, Temporal evolution of the normalized differential intensity of the peaks at (0 0 1) and (0 -1 3), respectively. The results are acquired at 30 K with a pump at $F = 2.5$ mJ/cm^2. **c, d**, Temporal evolution of the normalized differential FWHM along the in-plane direction of the peaks at (0 0 1) and at (0 -1 3), respectively. **e, f**, Temporal evolution of the normalized differential FWHM along the out-of-plane direction of the peaks at (0 0 1) and at (0 -1 3), respectively. The solid lines in all the panels are guides to eyes.

Supplementary Note 7. Time-dependent Landau theory simulations

Static Landau theory

Previous density functional theory (DFT) calculations have identified two unstable phonon modes in CsV_3Sb_5, which transform as the M_1^+ and L_2^- irreducible representations of the space group P6/mmm [15, 20, 21]. These phonon modes occur at three symmetry-equivalent reciprocal lattice vectors located at the three distinct M and three distinct L points in the hexagonal Brillouin zone. The vectors of M are:

$$Q_M^{(1)} = (0.5\ 0\ 0),\ Q_M^{(2)} = (0\ 0.5\ 0),\ Q_M^{(3)} = (-0.5\ -0.5\ 0), \tag{2}$$

and those of L are:

$$Q_L^{(1)} = (0.5\ 0\ 0.5),\ Q_L^{(2)} = (0\ 0.5\ 0.5),\ Q_L^{(3)} = (-0.5\ -0.5\ 0.5). \tag{3}$$

In real space, both M_i and L_i modes primarily involve nearest neighbour V-V bond contraction as shown in Fig. 1 in the main text, where the in-plane displacements of the V atoms account for over 90% of the total CDW displacements [20]. The distinction between M and L is in the relative phase of the displacements in consecutive kagome layers along the c-axis: the V atoms are displaced in-phase between the neighbouring layers for the M mode, while the displacement is out-of-phase between the neighbouring layers for the L mode. Clearly, each M_i forms a stripe pattern that doubles the unit cell along the stripe direction, while for L_i, the unit cell is also doubled along the c-axis.

The different "3Q" CDW structures correspond to distinct superpositions of three M_i and L_i CDW order parameters. We denote the phases formed by M and L modes using a general notation $M_1M_2M_3 + L_1L_2L_3$. A distortion with the opposite sign, namely an expansion of the V-V bond, is denoted as $\overline{M}$ or $\overline{L}$. For distortions where all the M or L order parameters have zero amplitude, we simplify the notation to $L_1L_2L_3$ and $M_1M_2M_3$, respectively. Also, we note that domains equivalent to each other up to a translation or rotation can be obtained as long as the sign of production $M_1M_2M_3$ and $L_1L_2L_3$ is preserved. For instance, $M_1M_2M_3 = \overline{M_1M_2}M_3$ and $L_1\overline{L_2}L_3 = \overline{L_1}L_2L_3$.

The Landau free energy functional for the coupled M_i and L_i order parameters is determined by symmetry, and its general form expanded up to the quartic order can be expressed as:

$$F = F_M + F_L + F_{ML}, \tag{4}$$

where

$$
\begin{aligned}
F_M =& \frac{\alpha_M(1 - T/T_M)}{2}M^2 + \frac{\beta_M}{3}M_1M_2M_3 + \frac{u_M}{4}M^4 + \frac{\lambda_M}{4}(M_1^2M_2^2 + M_2^2M_3^2 + M_1^2M_3^2), \\
F_L =& \frac{\alpha_L(1 - T/T_L)}{2}L^2 + \frac{u_L}{4}L^4 + \frac{\lambda_L}{4}(L_1^2L_2^2 + L_2^2L_3^2 + L_1^2L_3^2), \\
F_{ML} =& \frac{\beta_{ML}}{3}(M_1L_2L_3 + L_1M_2L_3 + L_1L_2M_3) + \frac{\lambda_{ML}^{(1)}}{4}(M_1M_2L_1L_2 + M_2M_3L_2L_3 + M_1M_3L_1L_3) \\
& + \frac{\lambda_{ML}^{(2)}}{4}(M_1^2L_1^2 + M_2^2L_2^2 + M_3^2L_3^2) + \frac{\lambda_{ML}^{(3)}}{4}M^2L^2,
\end{aligned}
\tag{5}
$$

where $M^2 = M_1^2 + M_2^2 + M_3^2$ and $M^4 = (M^2)^2$, with L^2 and L^4 defined analogously. α_M and α_L are the coefficients of the quadratic terms with tunable temperature T. Also note that since M_i and L_i belong to different irreducible representations, α_M and α_L are not necessarily identical, manifested as different transition temperatures T_M and T_L in the absence of coupling. Both α_M and α_L should be negative so that the ordered phase can be realized when $T < T_{M/L}$. u_M, u_L, λ_M, λ_L, $\lambda_{ML}^{(1)}$, $\lambda_{ML}^{(2)}$, and $\lambda_{ML}^{(3)}$ are the coefficients of the quartic terms. β_M and β_{ML} are the coefficients of the cubic terms.

One unambiguous feature of the functional is that while F_M and F_{ML} contain a trilinear term, F_L does not. This arises from the fact that different reciprocal lattice vectors of M_i and L_i obey different symmetries: $Q_M^{(1)} + Q_M^{(2)} + Q_M^{(3)}$ and $Q_M^{(1)} + Q_L^{(2)} + Q_L^{(3)}$ are zero modulo a reciprocal lattice vector, and thus the trilinear term is allowed. On the other hand, $Q_L^{(1)} + Q_L^{(2)} + Q_L^{(3)} \neq 0$, and thus the trilinear term $L_1L_2L_3$ is prohibited. Interestingly, this difference renders M more of a first-order nature, while L is more of second-order, as can be seen from F_M and F_L. This is also manifested in the different temperature dependence of the CDW superlattice peak intensity, where the peaks contributed exclusively by L exhibit a smoother increase at the transition while the peaks contributed by both show a

more abrupt increase due to the first-order characteristic of M (Supplementary Figure 2). Additionally, the presence of the trilinear term leads to $M_i \neq \overline{M_i}$, but its absence yields $L_i = \overline{L_i}$. One can intuitively understand this by examining the real-space CDW superlattice structure: $M_1 M_2 M_3 (+000)$ corresponds to a structure in which the two neighbouring kagome planes form aligned inverse star-of-David (soD) distortions, while $\overline{M_1} M_2 M_3$ corresponds to a distortion where the two neighbouring kagome planes form aligned soD patterns. These two superlattice structures are not necessarily energy-equivalent. However, both $(000+)L_1 L_2 L_3$ and $\overline{L_1} L_2 L_3$ correspond to different domains of the same superlattice with aligned alternative inverse soD and soD planes and are identical up to a translation along c-axis.

A combination of instabilities at M and L points finally leads to six possible $2 \times 2 \times 2$ CDW structures, namely $\overline{M_1} M_2 M_3$ (aligned soD), $M_1 M_2 M_3$ (aligned inverse soD), $L_1 L_2 L_3$ (aligned alternating inverse soD and soD), $\overline{M_1}00 + 0L_2 L_3$ (staggered soD), $M_1 00 + 0L_2 L_3$ (staggered inverse soD), and $M_1 M_2 0 + 00L_3$ (staggered alternating inverse soD and soD) [4]. Intriguingly, these states are not always thermodynamically stable in the presence of the trilinear coupling term β_{ML}. For instance, the $L_1 L_2 L_3$ phase is inevitably accompanied by a finite amount of $M_1 M_2 M_3$ or $\overline{M_1} M_2 M_3$ and becomes the $L_1 L_2 L_3 + M_1 M_2 M_3$ intertwined phase [20], which has been confirmed by the recent angle-resolved photoemission spectroscopy results [4]. Similarly, the $M_1 M_2 0 + 00L_3$ phase acquires additional M and L distortions from the two trilinear terms and cannot emerge as the leading instability [20].

All the Landau coefficients have been obtained from recent DFT calculations [1]: $\alpha_M = -2.53$ eV/Å^2, $\alpha_L = -2.53$ eV/Å^2, $\beta_M = -22.16$ eV/Å^3, $\beta_{ML} = -24.15$ eV/Å^3, $u_M = 76.43$ eV/Å^4, $u_L = 89.93$ eV/Å^4, $\lambda_M = -137.67$ eV/Å^4, $\lambda_L = -194.47$ eV/Å^4, $\lambda_{ML}^{(1)} = 347.73$ eV/Å^4, $\lambda_{ML}^{(2)} = 332.28$ eV/Å^4, $\lambda_{ML}^{(3)} = 24.20$ eV/Å^4. Based on these parameters, free energy landscape of different CDW structures can be simulated and a minimization of the free energy yields the values of the order parameters.

At zero temperature, $M_1 00 + 0L_2 L_3$ is found to have the lowest energy, in agreement with a wide array of experimental observations [2, 5, 6, 17, 22, 23]. At elevated temperatures, a reasonable choice of T_L and T_M (T_L=91 K and $T_M = 85$ K$< T_L$) predicts a ground state of $L_1 L_2 L_3 + M_1 M_2 M_3$, in line with another set of observations [4, 10, 24, 25]. The Landau theory simulations thus reproduce the two experimentally proposed CDW structures and demonstrate that they are energetically similar. For simplicity, we denote these two phases as MLL and LLL in the following discussions (MMM notation is dropped for $LLL + MMM$ because the M distortion is much smaller than the L distortion as shown shortly after, but the non-zero M is preserved). The Landau free energy for the two phases can be thus simplified as:

$$F_{MLL} = \frac{\alpha_M(1 - T/T_M)}{2} M^2 + \frac{u_M}{4} M^4 +$$
$$\frac{2\alpha_L(1 - T/T_L)}{2} L^2 + \frac{4u_L + \lambda_L}{4} L^4 + \tag{6}$$
$$\frac{\beta_{ML}}{3} ML^2 + \frac{2\lambda_{ML}^{(3)}}{4} M^2 L^2,$$

$$F_{LLL} = \frac{3\alpha_M(1 - T/T_M)}{2} M^2 + \frac{\beta_M}{3} M^3 + \frac{9u_M + 3\lambda_M}{4} M^4 +$$
$$\frac{3\alpha_L(1 - T/T_L)}{2} L^2 + \frac{9u_L + 3\lambda_L}{4} L^4 + \tag{7}$$
$$\frac{3\beta_{ML}}{3} ML^2 + \frac{3\lambda_{ML}^{(1)} + 3\lambda_{ML}^{(2)} + 9\lambda_{ML}^{(3)}}{4} M^2 L^2,$$

where for MLL we set $M_1 = M$, $L_2 = L_3 = L$, and for LLL, $M_1 = M_2 = M_3 = M$, $L_1 = L_2 = L_3 = L$.

The free energy landscapes of the aforementioned two phases are shown in Supplementary Figure 7a and Supplementary Figure 8a, respectively. Both potentials unambiguously depict an asymmetry along the M coordinate and a symmetry along the L coordinate due to the trilinear coupling terms, in agreement with our predictions. The MLL free energy potential shows two equivalent minima at both finite M and L and their distortion amplitudes are also nearly identical, i.e. $M \sim L$. This confirms that a staggered inverse soD ground state is energetically favorable. On the other hand, for the LLL free energy potential, the distortion amplitude of M is significantly smaller than that of L when the energy is minimized, in line with the angle-resolved photoemission spectroscopy results, where the former is 7 times weaker than the latter [4]. Also note that the coexistence of finite M and L indicates that they form intertwined order and are spatially homogeneous. The resulting structure is still an aligned alternating inverse soD and soD, but the in-plane distortion value is different for the two kagome planes ($L - M$ and $L + M$, respectively).

Time-dependent Landau theory simulations

We now derive the equations of motion for the order parameters. For the phenomenological treatment, whether M_i and L_i are lattice distortions or electronic order parameters of CDW is not critical, since they transform as the same irreducible representations. We assume they are electronic and thus display overdamped dynamics since on the phononic timescale, electrons nearly adiabatically adjust themselves to the local minimum of the Landau potential [26, 27]. The simulation results will not qualitatively change if we assume they are phononic and display second-order dynamics. To account for the phonon oscillation that exclusively occurs in L = half integer peaks, we introduce a lattice order parameter X in a harmonic potential, which primarily linearly couples to L and displays underdamped (second-order) dynamics [26, 27]:

$$F = F_{MLL/LLL} + F_X, \tag{8}$$

where

$$F_X = \frac{1}{2}\omega^2 X^2 + gXL, \tag{9}$$

where ω is the phonon frequency ($2\pi \times 1.3$ THz) and g is the electron-phonon coupling constant. Our approach by linearly coupling a phonon to L serves the exactly identical purpose as adding a phonon which only affects L=half integer peaks. The reason why we did not adopt the latter is because M and L involve V atom displacements, while previous literature has demonstrated the phonon we observed involves Cs atom motion (Note 5). Based on the principle of parsimony, we model the Cs motion as a linearly coupled phonon to L instead of involving additional atoms in the structure factor calculation.

We also assume that the photo-excitation acts as a homogeneous energy quench to the quadratic term $\alpha_{M/L}$, which is proportional to the pump fluence, while the other Landau parameters are independent on time:

$$\alpha_{M/L}(t) = \alpha_{M/L}(1 - T/T_{M/L})[1 - \kappa_{M/L}F\frac{(1 + \mathrm{erf}\frac{t}{\sqrt{2}t_r})}{2}(e^{-t/\tau} + C)]. \tag{10}$$

Here, F is pump fluence, $\kappa_{M/L}$ is a proportionality constant for normalizing F but they can be different for M and L, erf is the error function, t_r is the rise time of the quasiparticles after excitation, τ is the thermal relaxation time of the quasiparticles, and C is the long-term background constant within the simulation time window. The form of the time-dependent quench mimics the carrier excitation and relaxation dynamics measured by transient reflectivity experiments [15, 16].

Based on these assumptions, the dynamical equations of order parameters can be expressed as:

$$\frac{1}{\gamma_M}\partial_t M = -\frac{\partial F}{\partial M},$$
$$\frac{1}{\gamma_L}\partial_t L = -\frac{\partial F}{\partial L}, \tag{11}$$
$$\partial_t^2 X = -2\gamma_X \partial_t X - \frac{\partial F}{\partial X},$$

where γ_M, γ_L, and γ_X are phenomenological decay constants to account for damping of electronic and structural order parameters.

We first investigate the dynamics of the MLL phase. We assume $t_r = 0.1$ ps, $\tau = 1$ ps, $C = 0.9$, $\gamma_M = 1$ THz, $\gamma_L = 0.5$ THz, $\gamma_X = 0.2$ THz. The initial values of M, L, and X are set at their local minima. We also carefully choose the fluence regime and tentatively set $\kappa_M = 1$ and $\kappa_L = 3$, i.e. L is roughly three times more susceptible to light excitation than M to best reproduce the experimental results. The simulated temporal evolution of L and M normalized to their equilibrium values are shown in Supplementary Figures 7b and 7c, respectively. It is evident that neither of the two order parameters is fully quenched in this fluence regime, but L indeed shows a more substantial suppression than M. Additionally, the linearly coupled phonon exhibits a pronounced oscillation in L because of the linear coupling. However, due to the coupling between M and L, the oscillation also exists in M, albeit weakly.

Using the temporal evolution of M and L obtained from the simulation, we can calculate the dynamics of peak intensity $I(t)$ by incorporating their dynamics into the structure factor of different peaks: $\delta x_i(t)$ and $\delta y_i(t)$ can be expressed as a linear superposition of M and L. The simulated dynamics of each peak are shown in Supplementary Figures 7d-e. The peak at (0 -1.5 2.5) shows a considerable decrease accompanied by phonon oscillation upon

light excitation (Supplementary Figure 7d). This L = half-integer peak mainly reflects the dynamics of the L order parameter, as M can not generate L = half-integer peaks. In contrast, the peak at (-0.5 -1 2) exhibits a smaller intensity drop, while the peak at (0 -1.5 3) exhibits a drastic drop similar to the peak at (0 -1.5 2.5).

To emulate the measured intensity change, the dramatic penetration depth mismatch between the pump and the probe pulses at different wavelength ranges should be considered. Due to the pump-probe penetration depth mismatch, different depths z below the sample surface experience a different level of quenching of the potential. The reported pump and probe penetration depths are δ_{pu} =78 nm [28] and δ_{pr} =568 nm, respectively, which is approximately a seven-fold difference. To simulate the effects of the penetration depth mismatch, we assume the sample is composed of thin layers with thickness $d = 1$ nm and an exponential z-dependence of quenching with $F(z) = F \exp(-z/\delta_{pu})$ arising from an exponentially decaying photo-carrier distribution. We then solve the temporal evolution of $M(z, t)$, $L(z, t)$, and $I(z, t)$ for each layer. The probed-region-integrated value of $I_{int}(t)$ is calculated by summing over all the layers with each layer weighted by the probe penetration depth: $I_{int}(t) = \sum_{z=0}^{\infty} \exp(-z/\delta_{pr}) I(z, t)$. The integrated simulation results are shown in Figs. 2d and 2e. Supplementary Figures 7d-f can thus be understood as showing the dynamics of peak intensity from the top excited layer. A comparison between I_{int} and I reveals a 100% reduction of I should correspond to a nearly 18% drop in I_{int} (Supplementary Figure 13).

Although at first glance, it is plausible to attribute all three peaks to the MLL phase, two features suggest a different origin of the peak at (0 -1.5 3). First, the intensity drop observed in peaks (0 -1.5 2.5) and (0 -1.5 3) are very similar. After considering penetration depth mismatch, they are still quantitatively similar (Supplementary Figures 7g-i), whereas the experimental results show that the reduction of the latter is more considerably larger than the former. Second, since both order parameters are far from complete suppression, the simulated dynamics of all the peaks exhibit no clear features of dynamical slowing down of recovery time [27], at odds with the experimental observation of an apparent slowing down of dynamics at peak (0 -1.5 3).
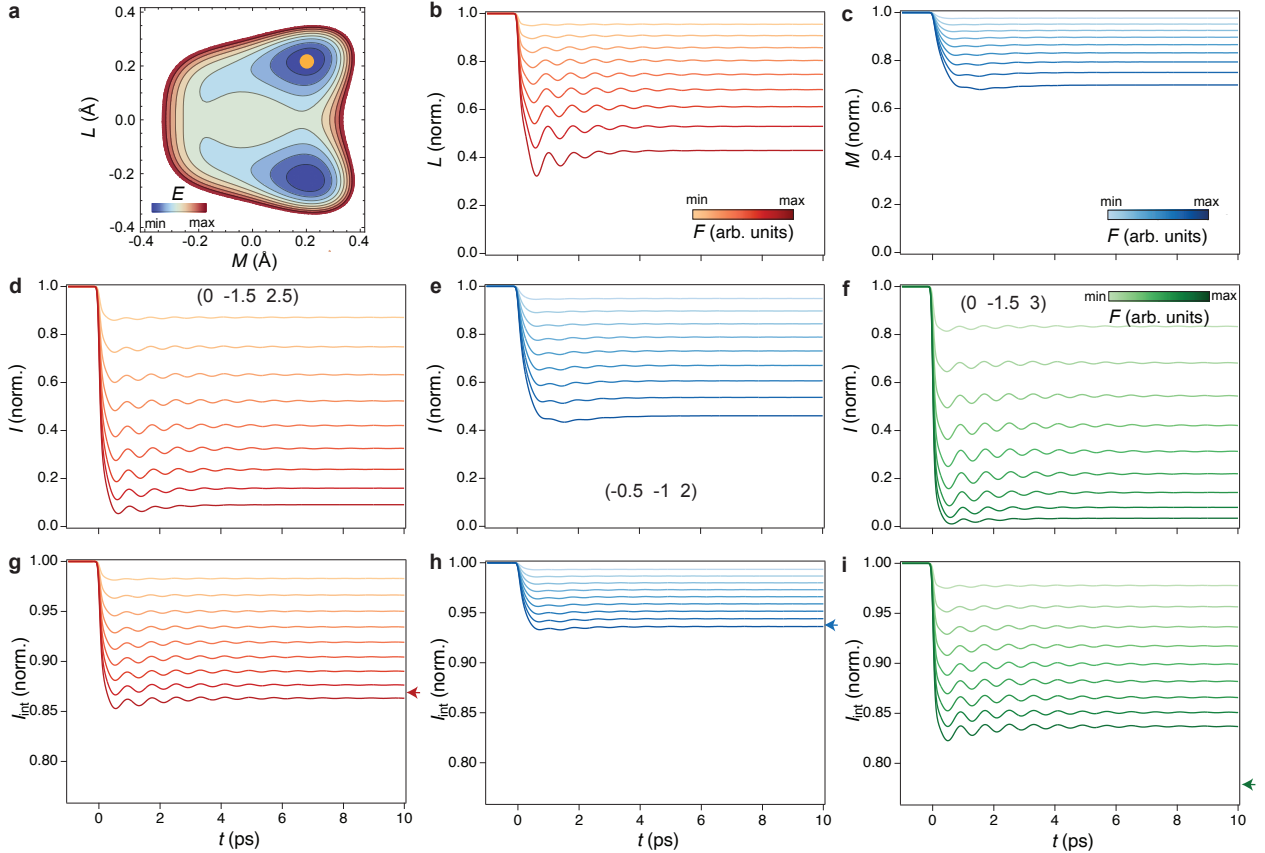
Supplementary Figure 7. **TDLT simulations of the MLL phase. a**, Free energy landscape of the MLL phase. The initial ground state is marked by a yellow dot. **b,c**, Temporal evolution of L and M order parameters at various fluences, respectively. **d-f**, Temporal evolution of intensity change of peak at (0 -1.5 2.5), (-0.5 -1 2), and (0 -1.5 3) at various pump fluences. **g-i**, Temporal evolution of the integrated intensity change of peak at (0 -1.5 2.5), (-0.5 -1 2), and (0 -1.5 3) at various pump fluences. The maximal intensity decrease measured experimentally are marked by arrows. The fluence range is identical in all the panels.
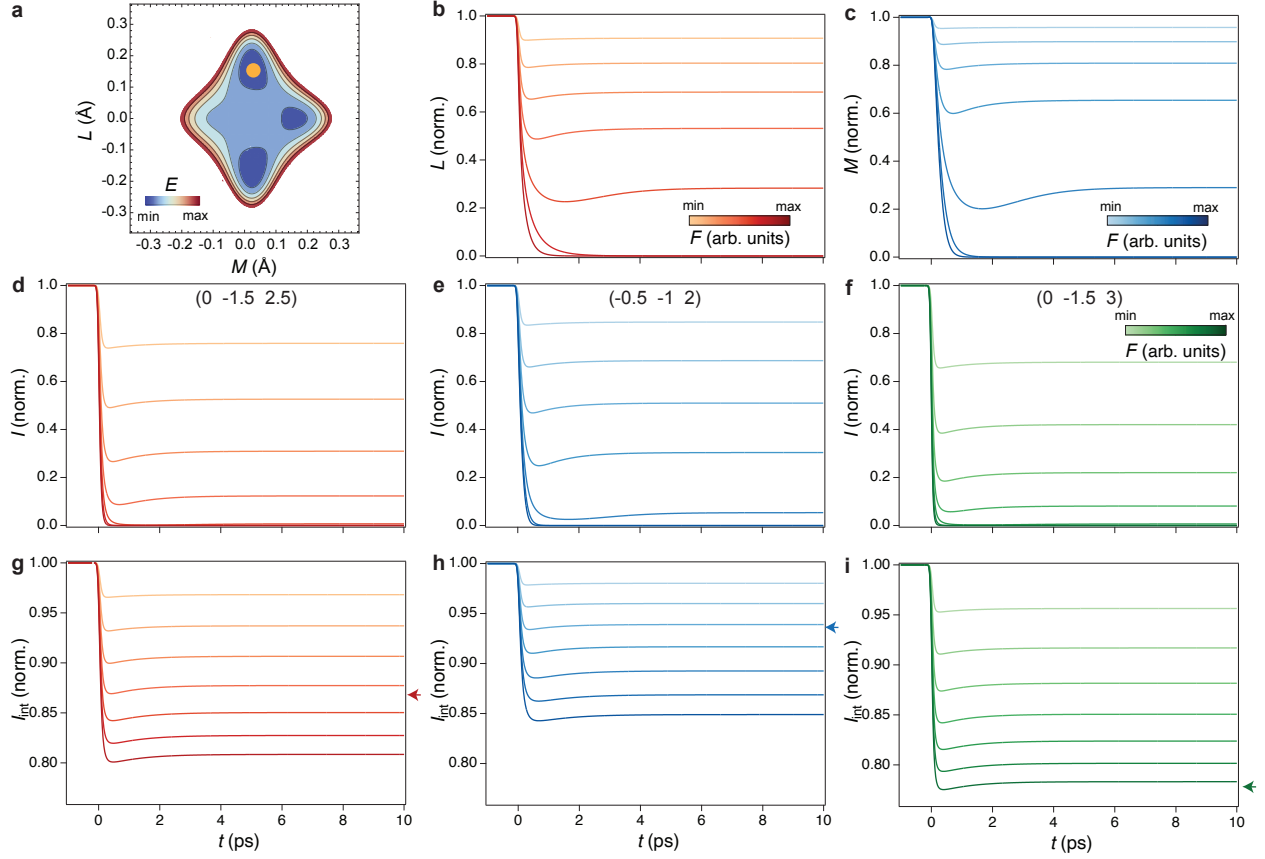
Supplementary Figure 8. **TDLT simulations of the** LLL **phase. a**, Free energy landscape of the LLL phase. The inital ground state is marked by a yellow dot. **b,c**, Temporal evolution of L and M order parameters at various fluences, respectively. **d-f**, Temporal evolution of intensity change of peak at (0 -1.5 2.5), (-0.5 -1 2), and (0 -1.5 3) at various pump fluences. **g-i**, Temporal evolution of the integrated intensity change of peak at (0 -1.5 2.5), (-0.5 -1 2), and (0 -1.5 3) at various pump fluences. The maximal intensity decrease measured experimentally are marked by arrows. The fluence range is identical in all the panels.

It is thus reasonable to suspect that the peak at (0 -1.5 3) may mainly originate from the LLL phase, since based on the structure factor calculation in Note 1, both structures can contribute to this peak with similar amplitude. To investigate this, we simulate the dynamics of M and L in the LLL phase (Supplementary Figures 8b and 8c). We explore the same fluence range employing the same set of parameters as we have used for MLL except for two: T_M, which we set to be $10K$, or at $T = 30$ K LLL will not be the global minimum but a local minimum, and g, which we set to be 0, since the peak at (0 -1.5 3) does not exhibit phonon oscillation within our resolution. However, we note that the absence of phonon should not be used as evidence for coexistence of two phases. We set $g = 0$ to better match the experimental observations here. Also note that although we show the normalized intensity change here, the absolute value of L is about 9 times larger than M, which matches the experimental value [4].

In contrast to the MLL case, despite the 3-times higher sensitivity of L in response to a light excitation, both M and L in LLL depict a similar level of melting at the same fluence and a complete melting of both is realized at an intermediate fluence. This may arise from the fact that the equilibrium value of M is so small that a moderate light excitation can fully quench it. In addition, a dynamical slowing down of the melting and recovery time can be observed at the critical fluence where both order parameters are completely quenched. Employing the same aforementioned method, we calculate the peak intensity dynamics $I(t)$ at the three peak positions (Supplementary Figures 8d-f) and include the pump-probe penetration depth mismatch to emulate the experimental case (Supplementary Figures 8g-i). Again, we note that the absolute equilibrium intensity of the peak at (0 -1.5 2.5) is two orders of magnitude smaller than the other two peaks and the same peak in the MLL phase, confirming that this peak should be predominantly contributed by the MLL phase. Although the absolute equilibrium intensity of the peak at (-0.5 -1 2) is similar to that of (0 -1.5 3) in LLL, its intensity is two orders of magnitude smaller than the same peak contributed by the MLL phase.

Dynamics of $I(t)$ also confirm that the first two peaks cannot mainly arise from LLL, because akin to M and L,

all the peaks show similar levels of intensity drop at the same fluence (Supplementary Figures 8d-i), in contrast to the dramatically different experimental behaviors. Moreover, all the peaks exhibit dynamical slowing down around the same fluence, which is absent in the experimental data. However, the behavior of peak (0 -1.5 3) qualitatively agrees with the experimentally measured dynamics, and the intensity drop in integrated $I_{int}(t)$ quantitatively agrees with the experimental value (Supplementary Figures 8i), demonstrating that the peak at (0 -1.5 3) mainly reflects the dynamics of the LLL phase.

We would like to note that despite its simplicity, the phenomenological TDLT simulation accurately predicts the dynamics of various peaks and disentangle the order parameter evolution of different phases. With almost no adjustable parameters in our calculation, it is encouraging to see a reasonable match in the absolute value of the CDW suppression between experiments and simulations. Indeed, a few ingredients can be further added to the model to improve its quantitative agreement with the measurements, such as fluence-dependent relaxation time τ, spatial inhomogeneity, and higher-order phonon couplings.

Robustness of the simulation results
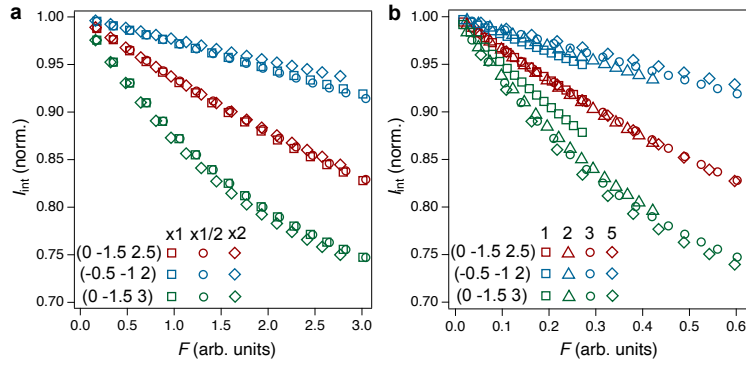
Supplementary Figure 9. **a**, Simulated fluence dependence of the normalized integrated intensity of the three peaks with all the microscopic parameters (α's, β's, u's, and λ's) equal to the values obtained from the first-principles calculations ($\times 1$), half of those values ($\times 1/2$), and double of those values ($\times 2$). All the dynamical parameters and the penetration depths are identical to the values that have been used in this note. **b**, Simulated fluence dependence of the normalized integrated intensity of the three peaks with κ_L/κ_M equal to 1, 2, 3, and 5. All the microscopic parameters, the other dynamical parameters, and the penetration depths are identical to the values that have been used in this note.

Here, we demonstrate the robustness of the TDLT simulation results against variations of the simulation parameters. The simulation parameters we employed can be categorized into three groups: 1) microscopic parameters α's, β's, u's, λ's, and T's determining the shape of the potential energy surface (PES) and equilibrium values of the order parameters M and L. These values are adopted from previous first-principles calculations [1]. Modifying them is expected to modulate the PES shape, while the peak intensity decrease should remain qualitatively similar with a scaling of the pump fluence. 2) dynamical parameters $\kappa_{L/M}$, t_r, τ, C, $\gamma_{L/M}$, ω, and g, which determine the rise time, decay time, oscillation frequency, oscillation damping time, and oscillation amplitude of the order parameters. Among these parameters, only $\kappa_{L/M}$ determines the photo-susceptibility (the amount of melting upon 1 mJ/cm^2 pumping) of M and L and thus the relative intensity drop of different peaks, while the others are less relevant to the magnitude of intensity decrease. 3) penetration depths of pump δ_{pu} and probe δ_{pr}, which are critical in determining the measured peak intensity decrease.

To assess the impact of parameter variations on peak intensity decreases, we performed more comprehensive TDLT simulations by considerably varying all three groups of parameters. In Supplementary Figure 9, we plot the simulated normalized integrated intensity I_{int} for the three targeted peaks with different sets of parameters as a function of the pump fluence F at $t = 0.5$ ps where the drop is maximal. To compare the relative intensity drops of different peaks between different sets of parameters, we apply a scaling factor for all the peaks along the pump fluence axis. This is valid because there exists a scaling factor between simulated and experimental pump fluence. Supplementary Figure 9a demonstrates that halving or doubling all the microscopic parameters minimally affects the relative magnitude of intensity decrease ($\sim$1%), in line with our expectation. Supplementary Figure 9b explores a large range of the ratio κ_L/κ_M, revealing qualitative consistency in peak intensity decrease of different peaks for $\kappa_L/\kappa_M \in (2, 5)$, with

$\kappa_L/\kappa_M \sim 3$ providing the closest agreement with experimental results. This confirms that L is more susceptible than M against photo-excitation and variations in dynamical parameters do not qualitatively alter the simulation results. As detailed in Supplementary Note 13, reasonable choices for penetration depths do not impact the peak dynamics qualitatively. Therefore, we can conclude that our simulation results quantitatively match the experimental values against even considerable variations in all the parameters.

Supplementary Note 8. Temporal evolution of the width of the peak at (-0.5 -1 2)

Temporal evolution of the width of the peak at (-0.5 -1 2) upon photo-excitation exhibits qualitatively similar features to that of the peak located at (0 -1.5 2.5) (Supplementary Figure 10). Moreover, the decrease in peak widths along both the in-plane ($\sigma_{//}$) and out-of-plane ($\sigma_{\perp}$) directions of (-0.5 -1 2) and (0 -1.5 2.5) show quantitative agreement. This observation suggests that both peaks possibly arise from the same CDW phase (MLL), even though there is a significant difference in the degree of reduction in peak intensity.
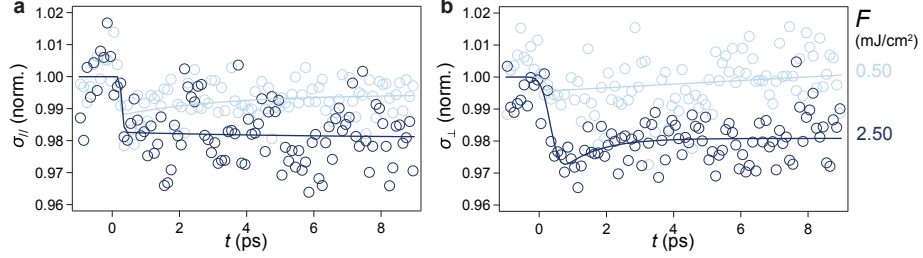

Supplementary Figure 10. **Temporal evolution of the width of the peak at (-0.5 -1 2). a,b**, Normalized width change of the peak at (-0.5 -1 2) along the in-plane and the out-of-plane directions, respectively, acquired at $F = 0.5$ and 2.5 mJ/cm^2. Solid lines are fits to a single-exponential decay.

Supplementary Note 9. Temperature dependence of the CDW peak width

Supplementary Figure 11 shows that the width of the CDW satellite peaks as a function of temperature around T_c = 91 K in the absence of the pump pulse. As shown by the normalized linecuts along $q_\perp$, the peak width increases as the temperature approaches T_c from below (Supplementary Figure 11a). We fit the linecuts of different peaks along both $q_\perp$ and $q_{//}$ directions with a Gaussian and obtain the half width at the half maximum (HWHM) $\sigma_{//}$ and $\sigma_\perp$ as functions of temperature (Supplementary Figures 11b-e). The width of all the investigated CDW peaks moderately increases when T approaches 90.5 K and quickly diverges when T approaches T_c, indicating a significant decrease in the correlation length of each CDW domain. This is in sharp contrast to the temporal dynamics of the peak width at (0 -1.5 2.5), where the peak width decreases after pumping. Therefore, we conclude that the anomalous photo-induced sharpening of the peak at (0 -1.5 2.5) is not due to a thermal effect.

Also we note that both $\sigma_{//}$ and $\sigma_\perp$ are presented in reciprocal lattice units (r.l.u.). We thus get the correlation length of the MLL phase at around 89 K is around 250 unit cells within the kagome plane and around 80 unit cells across the kagome plane, while the correlation length of the LLL phase is around 100 unit cells within the kagome plane and around 25 unit cells across the kagome plane. This indicates that the in-plane phase coherence of both phases is larger than their out-of-plane phase coherence, which is consistent with the out-of-equilibrium behavior where the out-of-plane stacking is more perturbed than the in-plane 2×2 distortions by a light excitation. Additionally, the MLL phase exhibits a longer correlation length than the LLL phase.
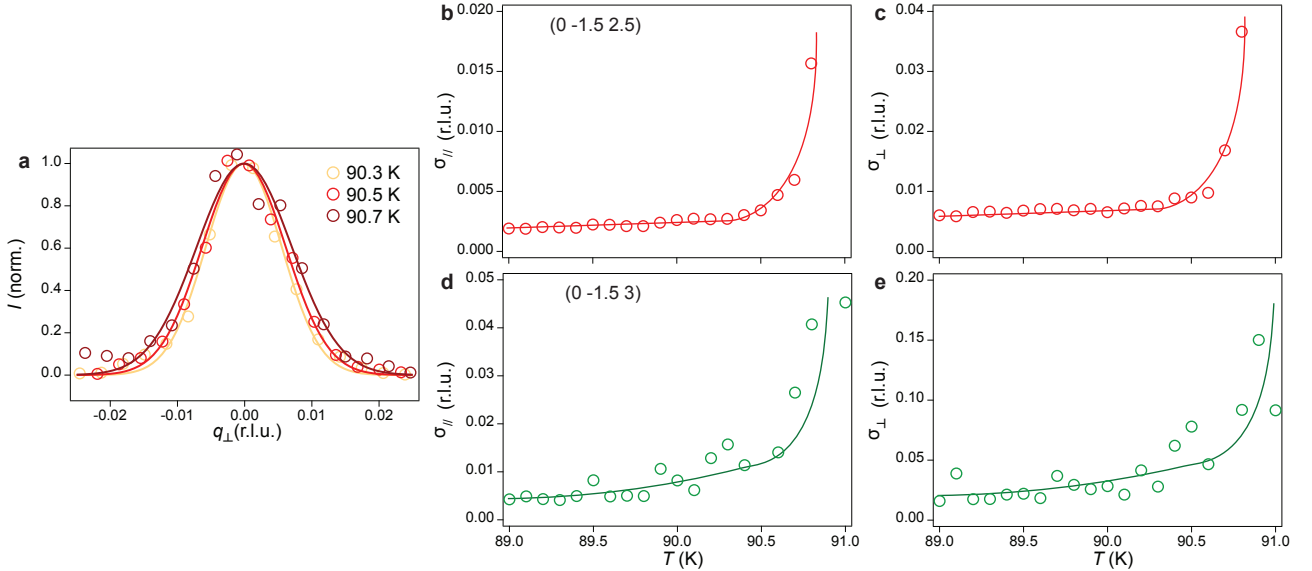
Supplementary Figure 11. **Equilibrium temperature dependence of CDW peak width near T_c. a,** Integrated linecuts of the peak at (0 -1.5 2.5) along $q_\perp$ direction at various temperatures near T_c= 91 K. Solid lines are fits to a Gaussian. **b,c,** Temperature dependence of the CDW peak HWHM at (0 -1.5 2.5) along the in-plane and out-of-plane directions, respectively. **d,e,** Temperature dependence of the CDW peak HWHM at (0 -1.5 3) along the in-plane and out-of-plane directions, respectively. Solid lines are guides to eyes.

Supplementary Note 10. Temporal evolution of the CDW peak position
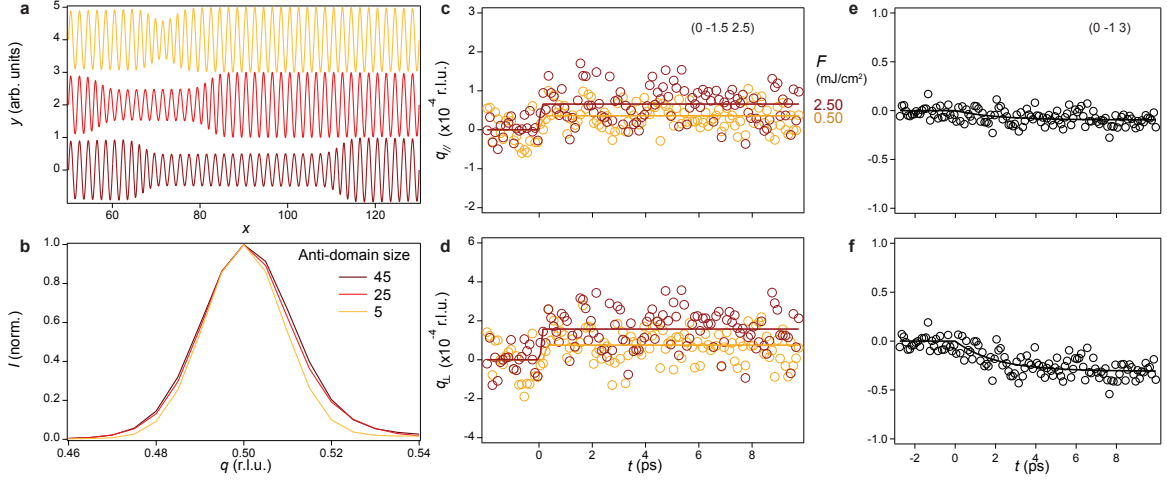
Supplementary Figure 12. **Temporal evolution of the CDW peak position. a,** Real-space configuration of the charge density with different sizes of anti-domain. Only a subset of the simulated region is shown for clarity ($50 < x < 130$). **b,** Normalized $|\text{FFT}|^2$ spectra of the CDW with different sizes of anti-domain. **c,d,** Temporal evolution of the peak position around (0 -1.5 2.5) along the in-plane and the out-of-plane directions, respectively. The data are acquired at $F = 0.5$ and 2.5 mJ/cm^2. Solid lines are fits to a single-exponential decay. **e,f,** Temporal evolution of the peak position around (0 -1 3) along the in-plane and the out-of-plane directions, respectively. The data are acquired at F=2.5 mJ/cm^2. Solid lines are guides to eyes.

We observe a subtle but noticeable peak position shift accompanied by peak width modulation, manifested as an asymmetric dip-peak-dip or peak-dip-peak feature in the differential linecuts shown in Fig. 3 in the main text. Note that not only is this shift almost instantaneous upon light excitation, in contrast to the slow modulation of Bragg peak position that reflects thermal expansion, but its amplitude is also nearly one order of magnitude larger than the thermal expansion in the same timescale (Supplementary Figures 12c-f). The peak shift at first glance may be counter-intuitive because in a commensurate CDW system, the charge order is strongly pinned to the lattice, making its periodicity highly robust against perturbation. However, as we show later in a toy model simulation, the peak position change does not necessarily indicate a reciprocal lattice vector change. Instead, a change in the CDW phase can modulate the peak position in the reciprocal space.

To illustrate this effect, we conduct a toy model simulation starting with a one-dimensional CDW order with a uniform phase $\phi = 0$. The order is present in a finite chain of 200 sites with a periodicity of 2 sites and a correlation length of 100 sites, mimicking the case of CsV$_3$Sb$_5$. We can express the real-space charge density modulation y as a Gaussian-enveloped sinusoid, i.e. $y(x) = A\sin(2\pi Qx + \phi)\exp\left[-\frac{(x-\frac{d}{2})^2}{2\sigma}\right]$, where $Q = 0.5$ is the reciprocal periodicity, $d = 200$ is the size, $\sigma = 100$ is the correlation length, $A = 1$ is the amplitude, and $\phi = 0$ is the phase. FFT indeed produces a peak centered at $q = 0.5$ with a finite width proportional to the inverse of σ.

Since the periodicity is 2, the CDW phase can be either 0 or π. Now without changing the periodicity, we introduce an anti-domain, i.e., a CDW domain with the same periodicity $Q = 0.5$ and opposite phase $\phi = \pi$. In the anti-domain, the phase increases from 0 to π at both edges in 2 sites but remains at π in the middle. We set the amplitude of the anti-domain to be half of the zero-phase domain and set the size of the anti-domain to be a value smaller than the correlation length of the dominant $\phi = 0$ CDW. Therefore, effectively both A and ϕ are functions of x in the 200 sites. The presence of these domains can be visualized in real space (Supplementary Figure 12a). Then we randomly set the position of this anti-domain within the 200 sites and calculate the FFT spectra. Further, we repeat this procedure 200 times to emulate the randomness of the anti-domains distributed in real space and sum over all the FFT spectra. Finally, we convolve the total spectrum with a Gaussian function representing the momentum resolution of the experimental instrument. The $|\text{FFT}|^2$ spectra of the anti-domains of different sizes are shown in Supplementary Figure 12b. Unequivocally, as the anti-domain size increases, both the peak width increase and a shift in the peak position away from $Q = 0.5$ can be observed, manifested as an asymmetric broadening. Note that this conclusion can be extended to higher-dimensional cases, and the results of the simulation will be qualitatively identical.

This toy model provides a qualitative demonstration that the modulation of the phase and amplitude of a CDW without changing its periodicity can lead to a shift in the corresponding momentum peak position and width. To be specific, the annihilation of $\phi = \pi$ domains within the dominant $\phi = 0$ region will induce a peak sharpening and position shift. In the case of CsV_3Sb_5, LLL surrounded by MLL can be considered as the anti-domain within the $\pi = 0$ domain. Therefore, along with the light-induced modulation of domain size, the peak position corresponding to different CDW phases will show a slight shift. Our simulation predicts that as the size of the anti-domain changes from 45 to 25 in the 200 sites, the peak width decreases by 3% and the peak position shifts by 0.0003 r.l.u. (Supplementary Figure 12b). Both values qualitatively match the experimental results, demonstrating that the two domains are mesoscopically separated rather than inhomogeneously entangled in real space (Supplementary Figure 12 and Fig. 3 in the main text) [29]. In addition, we indeed observe a larger peak shift along $q_\perp$ than $q_{//}$ (Supplementary Figures 12c and 12d), in agreement with the larger change in peak width along $q_\perp$.

Supplementary Note 11. Landau theory for two competing phases

We consider a system with two spacetime-dependent real order parameter fields $\Delta_1(r, t)$ and $\Delta_2(r, t)$. The general free energy functional F can be expressed as [30, 31]:

$$F[\Delta_1, \Delta_2] \propto \int d^D r (f_1[\Delta_1] + f_2[\Delta_2] + f_c[\Delta_1, \Delta_2]), \tag{12}$$

where $f_{1,2}$ characterizes the free energy of individual $\Delta_{1,2}(r, t)$, and f_c expresses the competition between the two orders where the presence of one would suppress the other such that the only stable minima are located at the $\Delta_1(r, t)$ and $\Delta_2(r, t)$ axes, i.e. one of them is zero. The free energy of both orders is assumed to be of first-order without loss of generality:

$$f_i[\Delta_i] = -\alpha_i(t)\Delta_i^2 + \beta_i\Delta_i^3 + u_i\Delta_i^4 + (\xi_i\nabla\Delta_i)^2. \tag{13}$$

Here α_i and u_i are positive while β_i is negative so the minima are realized when $\Delta_i > 0$. The cubic term makes the transition first-order (for the second order case, $\beta_i = 0$). $\xi_i > 0$ represents the correlation length. Only the quadratic term is modulated by light. The competition term has the form:

$$f_c[\Delta_1, \Delta_2] = c\Delta_1^2\Delta_2^2, \tag{14}$$

where c is large and positive.

Based on the aforementioned assumptions, the equilibrium global minima will be reached at

$$\Delta_{i,0} = \frac{-3\beta_i + \sqrt{9\beta_i^2 + 32u_i\alpha_i}}{8u_i}. \tag{15}$$

Minimizing f in one dimension with the boundary conditions $\Delta_1(x \to -\infty) = \Delta_{1,0}$, $\Delta_1(x \to \infty) = 0$, $\Delta_2(x \to -\infty) = 0$, and $\Delta_2(x \to \infty) = \Delta_{2,0}$, the domain wall profile can be approximated as [31]:

$$\Delta_i[x] = \Delta_{i,0}(\pm\tanh(x/\xi_{DW}) + 1)/2, \tag{16}$$

where $+/-$ corresponds to $i = 2$ and 1, respectively, and $\xi_{DW} \propto \xi/\sqrt{|\alpha|}$ characterizes the domain wall size.

We can also estimate the motion of interface between the two phases upon light excitation [31]. In the linear response regime, the displacement of a domain wall can be expressed as:

$$\Delta x = \frac{1}{d_0^2}\int dt[-\Delta_{1,0}^2(\alpha_1(t) - \alpha_1(0)) + \Delta_{2,0}^2(\alpha_2(t) - \alpha_2(0))], \tag{17}$$

where $d_0^2 \approx \frac{\alpha_1(0)}{u_1\gamma_1\xi_1} + \frac{\alpha_2(0)}{u_2\gamma_2\xi_2}$ and $\alpha(t)$ are given by Supplementary Equation 10.

This theory can be in principle used to capture the dynamics of our targeted system, where $\Delta_1(r, t)$ and $\Delta_2(r, t)$ represent the MLL and LLL phases, respectively, with the latter being more suppressed by light excitation. However, we need to treat each phase (MLL and LLL) described by a single order parameter, which contradicts with the general Landau theory employed in this system. Furthermore, all Landau parameters as defined before remain undetermined. Given the considerable uncertainty and arbitrariness, we refrain from modeling the competition between the two phases, as we deem the experimental observation sufficiently direct evidence.

Supplementary Note 12. Simulated and measured fluence dependence of the CDW peak intensity

In this note, we clarify the correspondence between the simulated and measured pump fluence dependence of the CDW diffraction peak intensity. We first show the simulation results. When the topmost single layer is 100% melted ($F \sim 1.7$, Supplementary Figure 13a), an $\sim18\%$ decrease of the integrated intensity across the probed region is reached (Supplementary Figure 13b). Since the pump has a finite penetration depth (~85 unit cells), further increasing the fluence leads to the complete melting of additional layers beneath the topmost layer. Therefore, the integrated intensity within the probe penetration depth continues to decrease (Supplementary Figure 13b). Specifically, the observed 22% decrease signifies the complete suppression of the LLL phase in the ~25 top layers at our highest experimental fluence. Also note that due to the significant pump-probe penetration depth mismatch, the integrated intensity does not exhibit a distinct saturation behavior as in the topmost layer when LLL is fully suppressed. Instead, only a change in photo-susceptibility (slope of I_{int} vs F) can be observed, as captured by our experiments (Fig. 2f and Supplementary Figure 14).
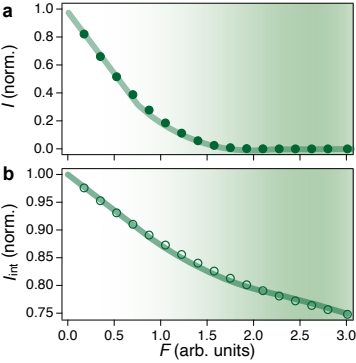
Supplementary Figure 13. Pump fluence dependence of the **a**, topmost layer intensity and **b**, integrated intensity within the probe penetration depth acquired at $t = 0.5$ ps from TDLT simulation of LLL. Thick lines are guides to the eyes. Shaded area denotes the region where the CDW of the topmost layer has been fully melted.

To experimentally examine the difference in photo-susceptibility between different order parameters M and L and different phases MLL and LLL, we conducted a finer pump fluence dependent measurement of the three peaks at $t = 0.5$ ps, where the intensity drop is maximized. Supplementary Figure 14 clearly shows that the photo-susceptibility of the (-0.5 -1 2) peak is ~3 times smaller than the (0 -1.5 2.5) peak, corroborating the ~ 3 times higher photo-susceptibility of L than M. Notably, both peaks do not exhibit clear saturation within the investigated fluence range. We refrain ourselves from reaching higher fluence to avoid sample damage, but an extrapolation would predict the saturation fluence to be higher than ~5 mJ/cm^2. On the contrary, the (0 -1.5 3) peak originating from LLL shows a ~2 times faster suppression and displays saturation behavior at ~2 mJ/cm^2 when the relative change is $\sim18\%$, consistent with the results in Fig. 2 and our simulation.
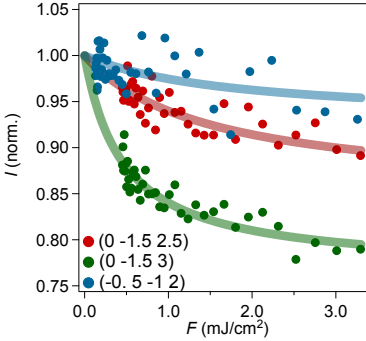
Supplementary Figure 14. Fluence dependence of the intensity drop of the three CDW peaks measured at $T = 30$ K and $t = 0.5$ ps. Thick colored lines are guides to the eyes.

Supplementary Note 13. Ruling out alternative possible interpretations

Mismatch in pump and probe penetration depths

It is worth noting that the probe penetration depth varies when we measure different peaks due to our experimental geometry. We used a six-axis diffractometer with θ (or η depending on the convention) = 2.95° [12], where the angle μ, which is close to but not exactly equal to the azimuthal rotation ϕ, is rotated to reach different diffraction peaks. Thus, as the sample is rotated, the incident angle β_{in} is not exactly equal to $\theta = 2.95°$, and thus the X-ray penetration depth is not constant. Therefore, it is possible that the disparity in penetration depths when measuring different peaks gives rise to the difference in the magnitude of peak intensity drop.

To quantitatively address this effect, we calculated the real X-ray incidence angles and corresponding penetration depths for the three CDW peaks: (0, -1.5, 2.5) peak: $\beta_{in} = 2.94°$, $\delta_{pr} = 564$ nm; (-0.5, -1, 2) peak: $\beta_{in} = 2.78°$, $\delta_{pr} = 534$ nm; (0, -1.5, 3) peak: $\beta_{in} = 2.89°$, $\delta_{pr} = 555$ nm. We find a $\sim$5% variation in X-ray penetration depth. Precisely, the intensity drops with accurate δ_{pr} values are 0.1%, 0.4%, and 0.3% larger than the intensity drops with an identical $\delta_{pr} = 568$ nm, corresponding to a constant $\beta_{in} = \theta = 2.95°$, for the (0 -1.5 2.5), (-0.5 -1 2), and (0 -1.5 3) peaks, respectively. These disparities cannot account for the difference in the measured intensity drop of different peaks, which are at least one order of magnitude larger. To induce an "artificial" difference solely from penetration depth mismatch between different peaks, a $\sim$55% variation in x-ray penetration depth would be required, which is impractically large. Therefore, we can confidently rule out the variation in β_{in} as the primary cause of the disparity in the amount of melting of different peaks.

The optical pump penetration depth could also vary as we rotate μ, if the sample is anisotropic in plane. Here, we show that the optical in-plane anisotropy of CsV_3Sb_5 is negligible for our measurement. First, the space groups of the MLL and LLL phases are $Fmmm$ (point group D_{2h}) and $P6/mmm$ (point group D_{6h}), respectively. The symmetry of the latter necessitates strict in-plane isotropy of the optical constant, while the former does not. However, previous Raman spectroscopy measurements on A_g and E_{2g} modes indicate no polarization-angle dependence both above and below T_c [18]. Additionally, no reports of in-plane anisotropy have emerged from optical conductivity measurements [28, 32]. These findings suggest negligible optical in-plane anisotropy, if any, when both phases coexist. Furthermore, we only moderately rotate μ by $\sim$15° to reach the three peaks. Therefore, the change in pump penetration depth due to the in-plane anisotropy is negligible when measuring the three peaks.

Static-strain induced spatial inhomogeneity of CDW domains

Assuming the coexistence of two CDW domains (MLL and LLL) and a static strain around the sample surface induced by cleavage, the CDW domain sizes around the surface can deviate from those in the deeper bulk. Since the surface domains are predominantly melted by light, the observed diffraction would primarily stem from the less perturbed bulk and the melting of only surface layers could result in a change in the measured peak width, which seems to explain the anomalous peak width alteration in our data. However, we provide four perspectives against this scenario as follows.

First, we note that the interlayer interaction in CsV_3Sb_5 is rather weak. We can easily exfoliate a few top layers off the sample with tape, instead of cleaving conventional 3D bulk samples by knocking off a post glued on the sample surface with epoxy. The weak interlayer coupling leads to inefficient strain transfer, and thus the strain induced by exfoliation, if any, should affect only a few layers near the sample surface. Moreover, investigations on AV_3Sb_5 using surface-sensitive techniques like angle-resolved photoemission spectroscopy (ARPES) and scanning tunneling microscopy (STM) show no evidence that cleavage alters the CDW distribution or structure, although cleavage has been routinely employed in these measurements.

Second, to more accurately assess the strain generated by exfoliation, we performed a toy-model calculation as illustrated in Supplementary Figure 15. In the mechanical exfoliation process, normal ($F_\perp$) and shear forces ($F_{//}$) are applied to the sample surface. With an order of magnitude estimate, both forces should not be over ~ 1 N. These forces will thus induce a pressure $P = F/A \sim 1$ N/(2 mm$\times$2 mm) ~ 0.0002 GPa, resulting in lattice deformation both perpendicular (ΔL) and parallel (Δx) to the sample surface. The magnitudes of the perpendicular ($\Delta L/L$) and parallel ($\Delta x/L$) strains are determined by the Young's modulus (E) and shear modulus (G) of the sample, which are around 89 and 33 GPa, respectively, based on DFT calculations [33]. These values yield $\Delta L/L = 0.0002\%$ and $\Delta x/L = 0.0006\%$, respectively. Given $L \sim 50$ μm, we have $\Delta L \sim 1$ Å and $\Delta x \sim 3$ Å. These values are even smaller than the dimension of one unit cell, which can hardly induce changes in the CDW domain sizes. Even if we assume

distortion occurs entirely in one domain, e.g. LLL, the relative change in domain size due to exfoliation along the two directions should be $\Delta L/\sigma_\perp \sim 1$ Å/23 nm = 0.4% and $\Delta x/\sigma_{//} \sim 3$ Å/55 nm = 0.5%, respectively. If light does not modulate the domain sizes of different CDW structures but merely melt the topmost domains, the expected change in the integrated peak width $\sigma_\perp$ and $\sigma_{//}$ within the probed region ($\sim$560 nm) would be both around 0.01%. This is at least two orders of magnitude smaller than our measured values ($\sim$12% and 3%, respectively). Consequently, the strain generated in the exfoliation process alone cannot account for the orders of magnitude larger peak width changes.
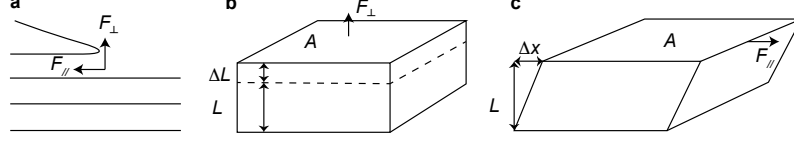
Supplementary Figure 15. Illustration of **a**, the forces generated in the exfoliation process, **b**, Young's modulus, and **c**, shear modulus.

For reference, previous experiments on CsV_3Sb_5 that investigated the change in T_c as a function of hydrostatic pressure [34–36] and uniaxial strain [37] also confirmed the negligible change in CDW induced by such a small strain/pressure. Specifically, with a pressure of 0.0002 GPa and 0.0006% strain, the anticipated relative changes in T_c should be around 0.001 K/91 K $\sim$ 0.001% and 0.0001 K/91 K $\sim$ 0.0001%, respectively.

Third, the temporal evolution of the peak width also provides evidence against this scenario. If the peak width change simply arises from the melting of the surface layers with different domain sizes, a synchronized change in peak intensity and width would be anticipated. To interrogate the initial changes in peak width and intensity, we closely examine their dynamics around time zero as shown in Supplementary Figure 16. We note that although the intensity decreases within $\sim$0.2 ps upon light excitation, potentially constrained by the time resolution, the peak width along both $q_{//}$ and $q_\perp$ directions shows a notable delay which continues to increase until $\sim$0.7 ps, a duration not limited by the temporal resolution. This temporal disparity unequivocally contradicts the proposed scenario.
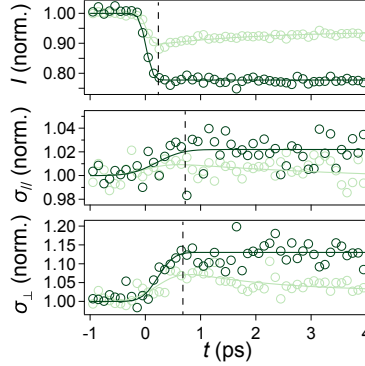
Supplementary Figure 16. Temporal evolution of the intensity and the width along $q_{//}$ and $q_\perp$ directions of the (0 -1.5 3) peak pumped at $F = 0.25$ (light green) and 2.5 mJ/cm^2 (dark green). Solid colored lines are fits to a single exponential decay. The vertical dashed lines denote the time delay when the transient changes of each variable starts to saturate or decay.

Last, we need to note that, although the relative changes in peak width along both $q_{//}$ and $q_\perp$ directions for the LLL peak are substantial, $\sim$3% and $\sim$12%, respectively, the absolute domain wall motion is not extensive, due to the relatively small static domain size of LLL, as demonstrated in Supplementary Note 9. The absolute domain wall motion along the two directions are $\Delta x = 100 \times 5.5$ Å$\times$3% = 16.5 Å and $\Delta z = 25 \times 9$ Å$\times$12% = 27 Å. The speed of expansion or contraction in domain size should be limited by the speed of sound. Inelastic X-ray scattering measurements and *ab initio* calculations have reported the speed of sound in CsV_3Sb_5 in a range from 2300 to 4600 m/s [7, 33]. Taking the mean value of 3400 m/s, the estimated time required for the domain wall motion along the two directions is $\sim$0.5 ps and $\sim$0.8 ps, respectively, qualitatively consistent with our experimental results as shown in Supplementary Figure 16. Therefore, our proposed mechanism of light-induced contraction of LLL domain and expansion of MLL domain indeed provides a persuasive explanation for our data.

Considering these perspectives collectively, we believe that our proposed scenario of phase competition better aligns

with our experimental observations. However, due to the limited signal-to-noise ratio of the peak width dynamics, we refrain from reaching quantitative conclusions about the exact timing of peak width changes in the main text.

Supplementary References

_____

* These authors contributed equally to this work
† email: gedik@mit.edu

[1] E. T. Ritz, R. M. Fernandes, and T. Birol, Physical Review B **107**, 205131 (2023).

[2] L. Kautzsch, B. R. Ortiz, K. Mallayya, J. Plumb, G. Pokharel, J. P. C. Ruff, Z. Islam, E.-A. Kim, R. Seshadri, and S. D. Wilson, Phys. Rev. Mater. **7**, 024806 (2023).

[3] S. Wu, B. R. Ortiz, H. Tan, S. D. Wilson, B. Yan, T. Birol, and G. Blumberg, Phys. Rev. B **105**, 155106 (2022).

[4] M. Kang, S. Fang, J. Yoo, B. R. Ortiz, Y. M. Oey, J. Choi, S. H. Ryu, J. Kim, C. Jozwiak, A. Bostwick, E. Rotenberg, E. Kaxiras, J. G. Checkelsky, S. D. Wilson, J.-H. Park, and R. Comin, Nature Materials **22**, 186 (2023).

[5] Q. Xiao, Y. Lin, Q. Li, X. Zheng, S. Francoual, C. Plueckthun, W. Xia, Q. Qiu, S. Zhang, Y. Guo, J. Feng, and Y. Peng, Phys. Rev. Res. **5**, L012032 (2023).

[6] Q. Stahl, D. Chen, T. Ritschel, C. Shekhar, E. Sadrollahi, M. C. Rahn, O. Ivashko, M. v. Zimmermann, C. Felser, and J. Geck, Phys. Rev. B **105**, 195136 (2022).

[7] H. Li, T. T. Zhang, T. Yilmaz, Y. Y. Pai, C. E. Marvinney, A. Said, Q. W. Yin, C. S. Gong, Z. J. Tu, E. Vescovo, C. S. Nelson, R. G. Moore, S. Murakami, H. C. Lei, H. N. Lee, B. J. Lawrie, and H. Miao, Phys. Rev. X **11**, 031050 (2021).

[8] H. Li, G. Fabbris, A. H. Said, J. P. Sun, Y.-X. Jiang, J. X. Yin, Y.-Y. Pai, S. Yoon, A. R. Lupini, C. S. Nelson, Q. W. Yin, C. S. Gong, Z. J. Tu, H. C. Lei, J. G. Cheng, M. Z. Hasan, Z. Wang, B. Yan, R. Thomale, H. N. Lee, and H. Miao, Nature Communications **13**, 6348 (2022).

[9] Q. Chen, D. Chen, W. Schnelle, C. Felser, and B. D. Gaulin, Phys. Rev. Lett. **129**, 056401 (2022).

[10] D. Subires, A. Korshunov, A. H. Said, L. Sánchez, B. R. Ortiz, S. D. Wilson, A. Bosak, and S. Blanco-Canosa, Nature Communications **14**, 1015 (2023).

[11] B. R. Ortiz, S. M. L. Teicher, Y. Hu, J. L. Zuo, P. M. Sarte, E. C. Schueller, A. M. M. Abeykoon, M. J. Krogstad, S. Rosenkranz, R. Osborn, R. Seshadri, L. Balents, J. He, and S. D. Wilson, Phys. Rev. Lett. **125**, 247002 (2020).

[12] H. You, Journal of Applied Crystallography **32**, 614 (1999).

[13] M. Mitrano, S. Lee, A. A. Husain, L. Delacretaz, M. Zhu, G. de la Peña Munoz, S. X. L. Sun, Y. I. Joe, A. H. Reid, S. F. Wandel, G. Coslovich, W. Schlotter, T. van Driel, J. Schneeloch, G. D. Gu, S. Hartnoll, N. Goldenfeld, and P. Abbamonte, Science Advances **5**, eaax3346 (2019).

[14] M. Trigo, P. Giraldo-Gallo, J. N. Clark, M. E. Kozina, T. Henighan, M. P. Jiang, M. Chollet, I. R. Fisher, J. M. Glownia, T. Katayama, P. S. Kirchmann, D. Leuenberger, H. Liu, D. A. Reis, Z. X. Shen, and D. Zhu, Physical Review B **103**, 054109 (2021).

[15] N. Ratcliff, L. Hallett, B. R. Ortiz, S. D. Wilson, and J. W. Harter, Phys. Rev. Mater. **5**, L111801 (2021).

[16] Z. X. Wang, Q. Wu, Q. W. Yin, C. S. Gong, Z. J. Tu, T. Lin, Q. M. Liu, L. Y. Shi, S. J. Zhang, D. Wu, H. C. Lei, T. Dong, and N. L. Wang, Phys. Rev. B **104**, 165110 (2021).

[17] Q. Wu, Z. X. Wang, Q. M. Liu, R. S. Li, S. X. Xu, Q. W. Yin, C. S. Gong, Z. J. Tu, H. C. Lei, T. Dong, and N. L. Wang, Phys. Rev. B **106**, 205109 (2022).

[18] G. Liu, X. Ma, K. He, Q. Li, H. Tan, Y. Liu, J. Xu, W. Tang, K. Watanabe, T. Taniguchi, L. Gao, Y. Dai, H.-H. Wen, B. Yan, and X. Xi, Nature Communications **13**, 3461 (2022).

[19] D. Azoury, A. von Hoegen, Y. Su, K. H. Oh, T. Holder, H. Tan, B. R. Ortiz, A. Capa Salinas, S. D. Wilson, B. Yan, and N. Gedik, Proceedings of the National Academy of Sciences **120**, e2308588120 (2023).

[20] M. H. Christensen, T. Birol, B. M. Andersen, and R. M. Fernandes, Phys. Rev. B **104**, 214513 (2021).

[21] M. H. Christensen, T. Birol, B. M. Andersen, and R. M. Fernandes, Phys. Rev. B **106**, 144504 (2022).

[22] Y. Xu, Z. Ni, Y. Liu, B. R. Ortiz, Q. Deng, S. D. Wilson, B. Yan, L. Balents, and L. Wu, Nature Physics **18**, 1470 (2022).

[23] L. Nie, K. Sun, W. Ma, D. Song, L. Zheng, Z. Liang, P. Wu, F. Yu, J. Li, M. Shan, D. Zhao, S. Li, B. Kang, Z. Wu, Y. Zhou, K. Liu, Z. Xiang, J. Ying, Z. Wang, T. Wu, and X. Chen, Nature **604**, 59 (2022).

[24] Y. Hu, X. Wu, B. R. Ortiz, X. Han, N. C. Plumb, S. D. Wilson, A. P. Schnyder, and M. Shi, Phys. Rev. B **106**, L241106 (2022).

[25] C. Li, X. Wu, H. Liu, C. Polley, Q. Guo, Y. Wang, X. Han, M. Dendzik, M. H. Berntsen, B. Thiagarajan, Y. Shi, A. P. Schnyder, and O. Tjernberg, Phys. Rev. Res. **4**, 033072 (2022).

[26] H. Schäfer, V. V. Kabanov, M. Beyer, K. Biljakovic, and J. Demsar, Phys. Rev. Lett. **105**, 066402 (2010).

[27] A. Zong, P. E. Dolgirev, A. Kogar, E. Ergeçen, M. B. Yilmaz, Y.-Q. Bie, T. Rohwer, I.-C. Tung, J. Straquadine, X. Wang, Y. Yang, X. Shen, R. Li, J. Yang, S. Park, M. C. Hoffmann, B. K. Ofori-Okai, M. E. Kozina, H. Wen, X. Wang, I. R. Fisher, P. Jarillo-Herrero, and N. Gedik, Phys. Rev. Lett. **123**, 097601 (2019).

[28] X. Zhou, Y. Li, X. Fan, J. Hao, Y. Dai, Z. Wang, Y. Yao, and H.-H. Wen, Phys. Rev. B **104**, L041101 (2021).

[29] S. Wandel, F. Boschini, E. H. da Silva Neto, L. Shen, M. X. Na, S. Zohar, Y. Wang, S. B. Welch, M. H. Seaberg, J. D. Koralek, G. L. Dakovski, W. Hettel, M. F. Lin, S. P. Moeller, W. F. Schlotter, A. H. Reid, M. P. Minitti, T. Boyle, F. He, R. Sutarto, R. Liang, D. Bonn, W. Hardy, R. A. Kaindl, D. G. Hawthorn, J. S. Lee, A. F. Kemper, A. Damascelli, C. Giannetti, J. J. Turner, and G. Coslovich, Science **376**, 860 (2022).

[30] Z. Sun and A. J. Millis, Phys. Rev. X **10**, 021028 (2020).

[31] Z. Sun and A. J. Millis, Phys. Rev. B **101**, 224305 (2020).

[32] E. Uykur, B. Ortiz, O. Iakutkina, M. Wenzel, S. Wilson, M. Dressel, and A. Tsirlin, Physical Review B **104**, 045130 (2021).

[33] M. Naher, M. Ali, M. Hossain, M. Uddin, and S. Naqib, Results in Physics **51**, 106742 (2023).

[34] F. Yu, D. Ma, W. Zhuo, S. Liu, X. Wen, B. Lei, J. Ying, and X. Chen, Nature Communications **12**, 3645 (2021).

[35] K. Chen, N. Wang, Q. Yin, Y. Gu, K. Jiang, Z. Tu, C. Gong, Y. Uwatoko, J. Sun, H. Lei, *et al.*, Phys. Rev. Lett. **126**, 247001 (2021).

[36] F. Yu, X. Zhu, X. Wen, Z. Gui, Z. Li, Y. Han, T. Wu, Z. Wang, Z. Xiang, Z. Qiao, *et al.*, Phys. Rev. Lett. **128**, 077001 (2022).

[37] T. Qian, M. H. Christensen, C. Hu, A. Saha, B. M. Andersen, R. M. Fernandes, T. Birol, and N. Ni, Physical Review B **104**, 144506 (2021).